# Corrosion resistance and tribological behavior of ZK30 magnesium alloy coated by plasma electrolytic oxidation

da Silva Rodrigues, Joel; Marasca Antonini, Leonardo; da Cunha Bastos, António Alexandre; Zhou, J.; de Fraga Malfatti, Célia

**DOI**
10.1016/j.surfcoat.2021.126983

**Publication date**
2021

**Document Version**
Accepted author manuscript

**Published in**
Surface and Coatings Technology

# Corrosion resistance and tribological behavior of ZK30 magnesium alloy coated by plasma electrolytic oxidation

Joel da Silva Rodrigues[a*], Leonardo Marasca Antonini[a], António Alexandre da Cunha Bastos[b], Jie Zhou[c] , Célia de Fraga Malfatti[a].

[a] LAPEC/PPGE3M, Universidade Federal do Rio Grande do Sul, Av. Bento Gonçalves, 9500, Prédio 43427, Sala 232, 91501-970 Porto Alegre, RS, Brasil,

[b] CICECO – Aveiro Institute of Materials and DEMaC – Department of Materials and Ceramic Engineering, University of Aveiro, 3810-193 Aveiro, Portugal

[c] Department of Biomechanical Engineering, Delft University of Technology, Mekelweg 2, 2628 CD Delft, The Netherlands.

## Abstract

The rapid bio-corrosion of magnesium-based alloys, the formation of hydrogen gas and, consequently, the premature loss of biomechanical functions hinder their applications as biodegradable implant materials. The corrosion becomes even accelerated, when fretting wear occurs at implant junctions, as a result of repeated disruptions of the magnesium (hydr)oxide layer formed on implant surfaces. To improve the overall performance of these materials in a bio-relevant environment, especially corrosion resistance and wear resistance, in this research, plasma electrolytic oxidation (PEO) was applied to create a coating on a magnesium alloy, ZK30. The resulting gains in corrosion resistance and wear resistance were evaluated. In vitro immersion tests in Hank's solution at 37 ºC showed a reduction in hydrogen release from the PEO-treated alloy. The results obtained from applying the scanning vibrating electrode technique (SVET) indicated a decreased susceptibility of the PEO-treated alloy to localized corrosion, accounting for the improved corrosion resistance. In addition, PEO was found to change the surface topography and roughness, in addition to surface chemistry, which

contributed to an increased but stable coefficient of friction and a decreased material removal rate, as revealed by the tribological tests with a ball-on-plate configuration. The results indicate an enlarged opportunity of magnesium-based materials for orthopedic applications, where friction and wear are involved, by applying PEO.

**Keywords:** Magnesium; Biodegradation; PEO; Corrosion; Wear.

## 1. Introduction

In recent years, magnesium-based materials have attracted the interest of researchers in their use as a new generation of biodegradable materials for bone-repair applications [1]. Most of magnesium alloy initially developed for structural applications can be divided into four main groups: pure Mg, the alloys containing aluminum (e.g., AZ31 and AZ91), the alloys containing rare earth elements (e.g., WE43) and the alloys without aluminum (e.g., Mg-Zn-based alloys) [2]. Among these alloys, Mg-Zn-based alloys stand out as potential biodegradable materials, considering their moderate-to-high strengths, due to the strengthening effect of zinc (Zn), and relatively low cytotoxicity, due to the absence of toxic elements, such as aluminum and rare earth elements [3]. Among the common Mg-Zn-based alloys, the ZK30 alloy contains about 3% zinc [4], while the ZK60 alloy contains about 6% zinc, which is meant to enhance the strengthening effect further [5] but compromises the corrosion resistance as a result of the formation of a large volume fraction of second-phase particles ($MgZn_2$), especially at grain boundaries and thus severe localized corrosion. In these alloys, zirconium (Zr) is present as the primary grain refiner and its biocompatibility is still controversial [6].

For bone-repair applications, it is necessary for a biodegradable implant material to maintain its biomechanical function during the bone healing period, typically up to 12 weeks [7]. The difficulty in performing the biomechanical function during such a period of time is due to the high corrosion rates of Mg-based alloys, correspond to the rapid formation of hydrogen gas, leading to gas accumulation in the region adjacent to the implant, interfering with tissue-implant interactions. Clearly, this difficulty can only be overcome by reducing the corrosion rates of Mg-based alloys to a level so low that the release of $H_2$ gas can be tolerated by the body [8]. A low biodegradation rate is even more difficult to attain and maintain, if the implant is subjected to relative motion with another object, leading to fretting wear [9]. Obviously, the key to solving all these difficulties lies in changing the surface chemistry,

mechanical properties and thus tribological behavior. A proper surface treatment can improve both the wear resistance and corrosion resistance [10]. Friction and wear have been more and more recognized as indispensable considerations in the design of medical devices and in the choice of biomaterials [11].

A large number of surface treatments, such as anodizing, conversion coatings, vapor deposition, polymer deposition and plasma oxidation, have been applied to light metals to increase corrosion resistance as well as wear resistance, mostly aiming at increasing the useful lifespan of these materials [12]. Among them, Plasma Electrolytic Oxidation (PEO), particularly suitable for light metals (Al, Mg and Ti) as valve metals, has been of special interest [13]. During the PEO process, a ceramic film grows on the surface of the metal through the oxidation of the substrate and also through the reduction and incorporation of chemical elements present in the electrolyte [14]. Being similar to anodizing, PEO is an electrolytic process, but being different from anodizing, a non-toxic, slightly alkaline electrolyte is typically used and a high potential is applied. The increased potential promotes the formation of millions of short-lived microscopic discharges, which fuse and modify the growing oxide layer, changing its structure and making it harder and denser over time. Different electrolytes and electrical regimes used in the PEO treatment of light metals can produce coatings with greater resistance to corrosion [15].

The formation of magnesium oxide films is due to diffusion of magnesium ions out of the interface and diffusion into the $SiO_3^{2-}$ interface. The film formation reactions would occur when the concentrations of these ions at the electrode/electrolyte interface reach a critical value [10]. The oxide coating is formed by a porous outer layer and a denser inner layer and has a porous reticulated structure that can be used as a model for the incorporation of lubricants, sealants, corrosion inhibitors and bone growth mediating proteins [16].

The barrier effect of the PEO coating, against corrosion, increases with the decrease in the average porosity values. These values are related to the treatment time and as the treatment time increases, the corrosion protection performance increases [17]. K.O. Gunduz et al. studied the influence of the percentage of zinc on the thickness of the coating obtained by PEO in an electrolyte containing $Na_2B_4O_7.10H_2O$. They found that a reduction in the thickness of the coating occurs with an increase in the percentage of zinc in Mg-Zn alloys [18]. The addition of Borate to the electrolyte benefits the growth of the PEO layer and the formation of the compact layer [19], increasing the barrier effect of the coating [20].

S. Lu et al. studied the effects of the addition of $Na_2B_4O_7$ on the thickness and wear resistance of a ZK60 magnesium alloy. They found that a concentration of 3g $L^{-1}$ of $Na_2B_4O_7$ in the electrolyte showed a better performance in relation to the growth of the layer [21]. The structure, composition, tribological and mechanical characteristics of a coating obtained by the PEO process on the ZK60 alloy were the object of study by S. Peibo et al. coating by the PEO process is an effective method for increasing the tribological performance of this alloy [22].

This study was aimed to evaluate the corrosion resistance and wear resistance of the ZK30 magnesium alloy coated by PEO. The coatings were obtained in a silicate-based alkaline electrolyte, free from fluoride in order to avoid possible toxicity stemming from $F^-$ ion release when the PEO surface layer is in contact with body fluids [23]. The initial comparisons were made with uncoated ZK30 and ZK60 alloy and this is a preliminary study for the possible application of these alloys as materials for bioabsorbable implants.

## 2. Experimental Details

### 2.1. Material preparation

The ZK30 and ZK60 magnesium alloys were prepared from high-purity Mg (99.95%), Zn (99.9%) and Mg–30Zr (wt%) master alloy. The raw materials were melted in an electric-resistance furnace under protection with an anti-oxidizing flux containing $MgCl_2$. After a grain-refining procedure at 760–800 ºC, the melt was poured into a steel mold preheated to 200–300 ºC. After solidification, rods were cut from the ingots and a surface layer was machined off to reach a diameter of 48 mm and a length of 200 mm. From the rods, samples with a cross section of 15 mm x 15 mm and a thickness of 3 mm were prepared. These samples were sanded with silicon carbide grinding papers up to grit 4000, polished with 1 µm diamond paste, cleaned in an ultrasonic bath with acetone, rinsed with deionized water, and finally dried with a cold air jet. The exact chemical compositions of ZK30 and ZK60 alloy slices determined using a Thermo Scientific Niton XL3t X-ray Fluorescent (XRF) Analyzer are given in Table I.

**Table I**

The ZK30 alloy had a density of 1.78 ± 0.02 $g\ cm^{-3}$, while the ZK60 alloy had a density of 1.84 ± 0.02 $g\ cm^{-3}$, determined by use of mass/volume ratio. The volume was measured with a MITUTOYO micrometer and the mass was measured with an analytical balance.

### 2.2. PEO treatment

The electrolyte used for the PEO treatment was composed of 17.5 g $L^{-1}$ sodium metasilicate, 4 g $L^{-1}$ potassium hydroxide and 3 g $L^{-1}$ sodium borate [24]. The volume of the electrolyte solution used was one liter. A 24 kW SUPPLIER brand alternating current source with frequency regulation and duty cycle was employed. The electrochemical cell used

consisted of a stainless steel counter electrode and the sample, as the working electrode, booth connect according to the circuit proposed by R.O. Hussein et al. [17].

The PEO anodizing time was 60 min, the working frequency 1000 Hz, the duty cycle 50%, and the maximum applied potential 240 V [13,25]. For data acquisition, a software package developed by SUPPLIER was used. PEO-treated ZK30 alloy samples were designated as ZK30PEO.

### 2.3. Evaluation and characterization

#### 2.3.1. In vitro biodegradation and corrosion behavior

Prior to in vitro immersion tests, samples were rinsed with distilled water and dried in open air. ZK30 and ZK60 samples were submerged in Hank's solution with a volume to area ratio of 40 mL $cm^{-2}$ and at a temperature of 36.5 ± 0.5 °C, according to the ASTM-G31-72 standard [26] and the procedure followed by X. Wei et al. [27]. The samples were subjected to the immersion tests for a maximum duration of 96 h. The electrolyte was refreshed every 24 h. At an interval of every 24 h, the samples were taken out of the solution and immersed in a chromic acid solution (200 g $L^{-1}$ $CrO_3$ + 10g $L^{-1}$ $AgNO_3$) for 2-3 min to remove the oxides [28], dried with a jet of cold air and weighed. At each immersion time point, the average corrosion rate was calculated from three samples:

$$v = \Delta m\ (S.t)^{-1} \qquad \textbf{Eq. 1}$$

where $v$ is the corrosion rate (g $m^{-2}$ $h^{-1}$), $\Delta m$ the mass change, $S$ the surface area of the sample before immersion, and $t$ the immersion time.

The calculated corrosion rates of the samples were verified by performing hydrogen evolution tests. The samples were soaked in Hank's solution at 37±1 °C under an inverted funnel connected to a graduated burette. The liquid level values in the burette were intermittently recorded at multiple time points up to 96 h. All the tests were performed in triplicate. Hydrogen evolution rate (HER), $V_H$ (mL $cm^{-2}$ $h^{-1}$), was calculated by using Eq. 2:

$$V_H = V\,(S.t)^{-1} \qquad \text{Eq. 2}$$

where $V$ is the measured hydrogen volume, $S$ the exposed area of the sample, and $t$ the soaking time [29,30].

The Scanning Vibrating Electrode Technique (SVET) was used to investigate the effect of microstructural features on the corrosion behavior of the samples in order to identify the main corrosion mechanism. The SVET instrument supplied by Applicable Electronics Inc. (USA) was controlled by the ASET 2.00 program developed by Science Wares (USA). The SVET microelectrode was prepared from polymer-isolated platinum-iridium microelectrodes, produced by Microprobes Inc. (USA). Scans were made at 100 µm from the surface. The microelectrode vibrated in two directions: one parallel ($x$-axis) to the sample surface and the other normal ($z$-axis) to the sample surface. The $x$ and $z$ frequencies were 115 and 69 Hz, respectively. The amplitude of vibrations in both directions was 10 µm. The measurement time at each point was 0.2 s. Maps with 50 x 50 points were obtained. A cell heating system was installed, which kept the electrolyte at 36.5 ± 1°C during the scan. The conductivity and pH of Hank's solution, used for the scans, were measured with an MP2021 SANXIN conductivity meter, which were 15.5 and 7.4 mS $cm^{-1}$, respectively. The measurements were made after 20 min, 4 h and 24 h of immersion in Hank's solution.

### 2.3.2. Tribological behavior and surface characterisics

Tribological tests were performed in a ball-on-plate configuration on a tribometer (CETR, USA) with linear and reciprocal movements by using a yttria stabilized zirconia ($Y_2O_3$/ $ZrO_2$) sphere with a diameter of 5 mm. A load of 2 N was applied for a period of 10 min, at an oscillation frequency of 1 Hz, and over a wear track length of 2 mm. For ZK30PEO specimens, the testing time was extended to 120 min. During the tests, tracks perpendicular to the polishing direction of the specimens were generated. All the tests in air were performed in

triplicate. After the tests, values of coefficient of friction (COF) were obtained and the wear rates determined. The images of the surfaces of the specimens and the tracks were obtained by using a GT-K optical interferometer (Bruker, Billerica, Massachusetts) with 0.95 x 1.26 mm analysis area and a scanning electron microscope (Zeiss EVO MA10 MEV) equipped with energy-dispersive X-ray spectroscopy (EDS). The spheres were coated with carbon to perform the analysis by EDS. An X-ray diffractometer (XRD) Philips equipment, model X'Pert MPD, was used, equipped with curved graphite monochromator and fixed copper anode, operating at 40 kV and 40 mA. Angle range analyzed from 5 to 75º and step used of 5º $s^{-1}$. Cu $K_\alpha$ (1.54184 Å), $K_{\alpha1}$ (1.54056 Å), $K_{\alpha2}$ (1.54439 Å) and $K_\beta$ (1.39222 Å) radiation.

The micrometric roughness values of the samples, i.e., the *Ra* (µm) and *Rz* (µm) values, were measured with a MITUTOYO SJ-400 profilometer. The measurements were performed in triplicate. *Ra* is defined as the arithmetic mean of the absolute values over the entire sampling length, while *Rz* is based on the five highest peaks and lowest valleys over the entire length.

## 3. Results and Discussion

### 3.1. In vitro degradation behavior of uncoated ZK30

The 96 h immersion tests in Hank's solution resulted in a much lower corrosion rate for the uncoated ZK30 alloy (0.355 ± 0.035 g $m^{-2}$ $h^{-1}$) than for the uncoated ZK60 alloy (0.683 ± 0.22 g $m^{-2}$ $h^{-1}$). This difference in corrosion rate indicated that the ZK60 alloy had a much greater susceptibility to corrosion in Hank's solution. It must have been associated with a higher concentration of zinc in ZK60 and thus the presence of an increased amount of second phase, favoring the formation of galvanic pairs with the magnesium matrix, as shown in the study carried out by Z. G. Huan et al. [31]. This is confirmed by the SEM micrographs and elemental analysis (Figure 1) of the surfaces of ZK30 (Figure 1a) and ZK60 (Figure 1b)

alloy samples, containing an intermetallic phase mostly at grain boundaries. The presence of the intermetallic phase was more pronounced in the ZK60 alloy than in the ZK30 alloy.

**Figure 1**

In connnection with the lower rate of mass loss of ZK30 samples, the ZK30 alloy showed lower $H_2$ evolution rates than the ZK60 alloy while being immerged in Hank's solution. As explained by L. Cui et al. [29], a decrease in $H_2$ evolution rate corresponds to the dissolution of the magnesium substrate and the formation of $Mg(OH)_2$ and $MgCO_3$ precipitates. As reported in the literature, excessive release of $H_2$ can lead to the formation of subcutaneous bubbles close to the implantation site, which can hinder cell adhesion and growth [32].

Figure 2 compares the degradation rates measured by using two different methods, i.e., mass loss and hydrogen evolution at 96 h immersion, both of which have been used to evaluate the biocorrosion behavior of magnesium-based alloys. With the mass loss method, the removal of (hydr)oxides from sample surface was carried out in the cleaning procedure prior to weighing, and this must have contributed to the higher values of corrosion rate compared to those determined by the evolution of hydrogen which might not be fully captured during the tests. Because it has a lower corrosion rate and, consequently, a lower evolution of hydrogen, only the ZK30 sample was used to obtain the coating by the PEO process.

**Figure 2**

### 3.2. Surface features of ZK30PEO

The surface of the coating created by PEO contained many micro-scale pores of different sizes and even a few cracks, as shown in Figure 3c. A similar morphology has been reported by other authors [33] and is believed to be associated with the type of the coating

process, during which the coating is generated with the formation of pores in the coating prevailing and with punctual dissolution points. The smaller pores are considered to be formed by ionic migration, while the larger ones result from the breakdown of the oxide layer [34]. As H. Li et al. [14] explained, the formation of micropores and cracking during the PEO process are due to the existence of micro-discharge channels, in which plasma generates fused oxides and regions with air bubbles due to high temperatures. The fused oxides are solidified and form a microstructure with micropores. The regions with microcracks in the coating occur due to the thermal stresses resulting from the rapid solidification of fused oxides [35]. The image taken on the cross section of the coating (Figure 3d) shows the presence of an inner layer, being more compact, and an outer layer, being more porous. Such PEO coating features have been observed by other researchers as well [34,36].

The creation of a ceramic layer by the PEO process aims to increase the resistance to corrosion and wear. However, a highly dense layer that can really act as an effective corrosion barrier would not be bioabsorable within a desired priod of time, making the implant similar to a permanent implant, which is not desirable. The micropores and microcracks present in the PEO coating may be possitively ultilized as transport channels to allow the permeation of the body fluids to the substrate, while the rest of the coating decreases the exposed area of the substrate and, consequently, decreases the corrosion rate and hydrogen release. This consideration is shared by V. Dehnavi et al. [37] who used the PEO process to form a ceramic surface with crystallinity on magnesium alloys, having a greater hardness value and a more stable surface to resist corrosion and wear. On the other hand, as M. Dabala et al. [38] pointed out, the presence of excessive pores and cracks on the PEO surface could reduce the wear resistance of magnesium alloys.

XRD analysis (Figura 3b) showed that the PEO coating was predominantly composed of magnesium silicate ($Mg_2SiO_4$), silicon dioxide ($SiO_2$) and magnesium oxide (MgO). A similar phase composition was found by P. Zhang et al. [39] who identified amorphous and

crystalline phases, i.e., MgO, $Mg_2SiO_4$, and $Mg_3(PO_4)_2$. In addition, the authors pointed out that the phase composition of the PEO coating depends on the mode of the applied current, the current density, and the composition and concentration of the electrolyte, in addition to the PEO treatment time. The formation of $Mg_2SiO_4$ makes the film more uniform and has better properties against to corrosion [40]. S. Durdu et al [41]. studied the morphology of the different phases in the coating obtained by the PEO process in samples of pure commercial Magnesium. They found that, in silicate solution, the increase in current density caused a greater formation of the $Mg_2SiO_4$ phase, making the film more compact and with greater resistance to corrosion.

EDS mapping of magnesium and silicon on the PEO coating cross section is shown in Figure 3d. It is clear that the presence of Mg was predominant and it was distributed homogeneously across the coating, while the presence of silicon occurred only in the outer layer. The same elemental distributions were observed by L. Zhu et al. [34]. The coating created in this study on the ZK30 alloy had a thickness of 17.8 ± 6.3 µm (Figure 3d). V. Dehnavi et al. [37] obtained different layer thicknesses in a concentrated alkaline electrolyte by applying low voltages (150 - 450 V) on the AM50 magnesium alloy. The authors found that micro discharges became stronger as time was extended and that the coating thickness depended on the concentration of the electrolyte and the time of the PEO process.

**Figure 3**

The micrometric roughness data (Table II) before and after PEO showed that the application of the ceramic coating on the ZK30 alloy increased the *Ra* and *Rz* values. It indicated that the coating changed the surface topography, which is in agreement with the SEM observation (Figure 3) that PEO created a more heterogeneous surface with the presence of micropores and cracks (Figure 3c). The increases in roughness values (*Ra* and *Rz*) of the

ZK30PEO sample were caused by micro discharges on the surface of the substrate (Figure 3a), which is typical of the PEO process involving rapid melting and solidification of the base material, which could increase the roughness of the surface, as observed by Y. Savguira et al. [42]. R.O. Hussein et al. [43] studied the coating growth mechanisms and ascribed the discharge events during the process to be those that originated the metal-oxide interface. The discharges resulted in a porous coating structure with cracks, which could decrease the resistance to corrosion, as the electrolyte could penetrate the coating and cause corrosion at the metal-oxide interface.

**Table II**

### 3.3. In vitro degradation behavior of ZK30PEO and main corrosion mechanism

To determine the in vitro degradation rates, ZK30PEO samples were subjected only to the hydrogen release tests, since the mass loss method used to determine the corrosion rates of uncoated ZK30 samples involved the removal of oxides by chromic acid. This method could cause damage to the PEO coating layer. As shown by M. Liu et al. [44], G. Song et al.[45] and G. Song et al. [46], when magnesium is in contact with a corrosive electrolyte, the Mg anodic reaction occurs and, as a result, the cathodic $H_2$ production reaction follows ($Mg + 2H^+ = Mg^{2+} + H_2$). These reactions open up the possibility of measuring the magnesium corrosion rate by monitoring the release of hydrogen.

ZK30PEO samples exhibited much lower $H_2$ evolution volumes than the uncoated ZK30 alloy counterparts (Figure 4) at all the time points, indicating that the PEO coating indeed acted as a barrier between the substrate and the medium, slowing down the corrosion process of the ZK30 alloy and, consequently, the $H_2$ evolution. Y. Xin et al. [47] and E. Zhang et al. [48] stressed the importance of controlling the $H_2$ release, because rapid release of hydrogen gas could hinder the formation of a layer composed of magnesium and calcium phosphate. Such a layer would have the ability to protect the substrate from rapid corrosion

and could facilitate the osteoconductivity when the magnesium alloy would be used as an orthopedic implant material.

**Figure 4**

The SVET tests of ZK30PEO samples and uncoated ZK30 samples revealed the points or regions with variations in corrosion density value, thereby showing the progressive corrosion of the samples over the time of immersion (Figure 5). From Figure 5, it is clear that during the first 4 h of the testing, the uncoated ZK30 sample had isolated points of corrosion with low current density (Figure 5a2). After 24 h, the same sample (Figure 5a3) showed anode current peaks. These peaks must have been associated with a high percentage of the zinc-containing phase present in the sample. The zinc-containing phase present in the grain boundary regions could act as a cathode and the magnesium present in the matrix could act as an anode, forming anodic and cathodic regions on the sample surface.

D. Kajánek et al. [20] studied samples of the AZ31 magnesium alloy with PEO coating using the Kelvin Probe (SKP) Scanning technique and found that the coating obtained by PEO showed a significant improvement in corrosion resistance compared to samples without coating, which points to an effective barrier character against corrosion. They also found that the induction of an artificial scratch on the surface of the coating changed the mechanism of corrosion. The artificial defect acted as an anode with higher potential values compared to the surrounding PEO coating. Corrosion products protected the substrate and acted as a barrier that reduced the anodic reaction. They observed that the PEO coating near the corrosion products started to dissolve and became an anode in the corrosion pair. Therefore, there is an option that if the PEO coating is damaged in a particular location, this location can be partially and temporarily protected by this corrosion products and the PEO coating is playing a sacrificial anode role. It is important to note that this behavior was not

observed in this work, probably due to the immersion time of the sample. The Svet map (Figure 5c3) showed small anodic regions and large cathodic regions and this may be linked, initially, to the barrier effect of the coating, preventing the contact of the electrolyte with some regions of the substrate.

The current maps of ZK30PEO (Figure 5c1 and Figure 5c2) showed no active regions of localized corrosion until 4h of immersion, indicating that, to a great extent, the coating acted as a barrier between the substrate and the medium and protected the ZK30 substrate from localized corrosion. Only after 24h of immersion in Hank's solution, the ZK30PEO sample showed small regions with raised current density (Figure 5c3), although the value was lower than that of the uncoated sample (Figure 5a3). It became clear that, despite the presence of micropores and cracks on the PEO surface, the PEO coating could effectively reduce the exposed area of the substrate, prevent the extensive contact of the substrate with the electrolyte, and thus present a lower current density overall on the sample surface. Wang et al. [49] compared the corrosion behaviors of the PEO-treated and uncoated 7075 aluminum alloy by using SVET and found that the current density on the uncoated alloy surface first increased and then decreased. Such behavior was attributed to the formation of corrosion products. It was also found that the creation of the ceramic coating by PEO significantly decreased the current density on the sample surface, thus exhibiting a desired barrier behavior.

**Figure 5**

### 3.4. Tribological behavior of ZK30PEO

The micropores present in the PEO coating could allow plastic deformation under small mechanical loading, thus preventing cracks from spreading during tribological tests involving sliding motion. Z. Li et al. [50] studied the wear performance of ceramic coatings created by PEO on a magnesium alloy and found that the size of pores directly influenced the

wear resistance; ceramic coatings with smaller and more regular pores created during PEO at higher potentials showed better performance in terms of corrosion and wear resistance.

The tribological tests performed in the present research show that the values of coefficient of friction (COF) of ZK30PEO (Figure 6a) were almost consistently higher than those of the uncoated ZK30 and ZK60 alloys. Clearly, the increased values of COF must have been associated with higher micrometric roughness values (Table II). The only exception was at the beginning of the tribological tests. The COF value quickly increased and then gently increased till the end of the test at 600 s. This behavior is very similar to that found in the PEO coatings on the MRI 230D magnesium alloy and explained by G. Rapheal et al.[35] in terms of the continuous renewal of sample contact area. An increase in surface roughness as a result of an extended PEO treatment time, influencing the wear behavior of samples, was found by A. Buling et al. [51]. It was also observed that more homogeneous pores, obtained by changing PEO process parameters, led to smaller deviations in roughness values and an increase in resistance to corrosion and wear.

In addition to surface roughness, the tribological behavior is related to the mechanical properties of the PEO coating. W. Xue et al. [52] and A.L. Yerokhin et al. [53] found the oxide layers created by PEO on magnesium alloys very hard and well bonded to the substrate. The PEO coating on magnesium alloys is composed of two sub-layers, an outer layer with relatively low mechanical properties, corresponding to relatively lower wear resistance, and an inner layer, which is a compact layer between the porous outer layer and the substrate and has better mechanical properties. Considering the coating structure and the higher COF values relative to those of the uncoated alloy, it could be inferred that the compact layer contributed to the improved wear resistance of ZK30PEO. The gradual increases in COF over time after the first 100 s (Figure 6a) could be caused by the exposure of the inner compact layer, after the outer layer was removed during the running-in period. The smaller fluctuations of the COF values of ZK30PEO, in comparison with the curves of the uncoated samples (Figure 6a)

were considered to be related to the operating wear mechanism. For the PEO coated samples, the wear mechanism appeared to be predominantly abrasive, while for the uncoated samples it must have been predominantly adhesive. In the study conducted by G. Rapheal et al. [35], the uncoated magnesium alloys showed greater fluctuations in the COF graphs, similar to the results obtained in our study (Figure 6a), which was attributed to the softening wear behavior, followed by irregular sliding.

Samples of ZK30 (Figure 6b1) and ZK60 (Figure 6b2) showed streaks along the wear track, indicating adhesion of material in the sphere, as evidenced by the micrographs of the counter specimens (Figure 6c1 and Figure 6c2). This wear track characteristic was, however, not observable in the wear track formed on ZK30PEO sample (Figure 6b3). The appearance of the wear track of ZK30PEO sample and the counter specimen with little adhered material (Figure 6c3) suggested abrasion to be the predominant wear mechanism.

**Figure 6**

The process of adhesive wear and the occurrence of material delamination, due to surface fatigue, could be clearly observed in ZK30 and ZK60 samples (Figure 7). The observation is similar to that of H. Chen et al. [54]. The counter specimens of ZK30 (Figure 7b1) and ZK60 samples (Figure 7b2), analyzed by means of SEM/EDS, had material adhered to the sphere surface and containing magnesium, zinc and zirconium, which confirmed the main wear mechanism to be adhesive. Because no changes during the tribological tests for 10 min were observed, the SEM/EDS analysis of the ZK30PEO wear track and counter specimens was performed only at the testing time of 120 min, as shown in Figure 8. By that time, material transfer from ZK30PEO to the counter specimen also occurred, although to a less extent. However, strong oxide signal remained on the specimen surface, indicating the ceramic layer was not worn out.

**Figure 7**

**Figure 8**

The ZK30 alloy exhibited a greater track width (Figure 9a) than the ZK60 alloy (Figure 9b), indicating a greater amount of material removed. This result is in agreement with the images of the surface of the spheres, obtained by optical microscopy, in which the ZK30 alloy transferred more material from its surface to the sphere, since there was more material adhered to its surface (Figure 6c1).

After applying the PEO coating on the ZK30 alloy, a marked decrease in the volume of material removed was noted (Figure 9b), as well as an obvious decrease in the amount of material transferred from the coating surface to the sphere (Figure 6c3). This observation indicated that the coating contributed greatly to increased wear resistance, corroborating the finding of X. Li et al. [55] that the PEO coating enhanced wear resistance.

**Figure 9**

With the extension of the tribological test time to 120 min, COF value of ZK30PEO gradually increased from 0.6 to 0.8 and then became stabilized (Figure 10a). These values were much higher than the values of the uncoated materials, which fluctuated around 0.3 to 0.4 (Figure 6a). In addition, even after 120 min of the tribological testing, the PEO coating did not exhibit complete rupture, which would otherwise lead to the direct contact of the counter specimen with the substrate, since there was no abrupt drop in COF to the values close to those of the substrate. From Figure 10c, it can be seen that after 30 min of the tribological test, cracks started to be visible on ZK30PEO specimen surface. This must have been related to the removal of the most porous outer layer. With extension in tribological test time to 60

min and then to 120 min, wear debris accumulated on the surface and in the regions of rupture of the PEO coating, leading to third-body abrasive wear, as described earlier in identifying the operating wear mechanism in the case of ZK30PEO.

**Figure 10**

## 4. Conclusions

The coating created by PEO on the ZK30 magnesium alloy enhanced the corrosion resistance and wear resistance. The PEO coating was composed of silicon- and magnesium-containing oxides. Optical interferometry indicated increase in micrometric roughness and the presence of micropores and cracks on the PEO coating surface. ZK30PEO exhibited increased corrosion resistance in Hank's solutions and decreased hydrogen evolution, as compared to the uncoated ZK30 alloy. Surface analysis by means of SVET showed that the ZK30PEO alloy was less susceptible to localized corrosion. In the tribological tests, increased and stable values of coefficient of friction were measured, along with a smaller amount of material transferred from ZK30PEO to the counter specimen. The results obtained from this study clearly demonstrated the improved corrosion and wear resistance of the ZK30 magnesium alloy by applying PEO coating and the new potential for PEO-coated magnesium alloys to be used as biodegradable materials.

**Credit authorship contribution statement**

Joel da Silva Rodrigues: *Methodology, Investigation, Writing – original draft*

Leonardo Marasca Antonini: *Investigation, Writing – original draft*

António Alexandre da Cunha Bastos: *Methodology, Investigation, Writing – review*

Jie Zhou: *Writing – Conceptualization, review*

Célia de Fraga Malfatti: *Conceptualization, Supervision, Formal analysis.*

**Declaration of competing interest**

The authors indicated no potential conflicts of interest.

**Acknowledgments**

The present work was conducted with the support of CAPES, a Brazilian Government entity focused on human resources qualification, with the support of CNPq and CAPES – PROEX (Process 23038.000341/2019-71). C. F. Malfatti acknowledges CNPq (Grant 307723/2018-6), and L.M. Antonini thanks for Postdoctorate scholarship CAPES PNPD (Grant PNPD20132547).

**Funding Sources**

This research did not receive any specific grant from funding agencies in the public, commercial, or not-for-profit sectors.

**References**


[1] A. Mahapatro, S. A. Arshanapalli, Bioceramic Coatings on Magnesium Alloys, Journal of Bio- and Tribo-Corrosion (2017) 3-37. https://doi.org/10.1007/s40735-017-0099-7.

[2] L. Aljihmani, L. Alic, Y. Boudjemline, Z. M. Hijazi, B. Mansoor, E. Serpedin, K. Qaraqe, Magnesium-Based Bioresorbable Stent Materials: Review of Reviews, Journal of Bio- and Tribo-Corrosion (2019) 5-26. https://doi.org/10.1007/s40735-019-0216-x.

[3] Sharma-Persaud, D., Mcgoron, A. J., Biodegradable Magnesium Alloys: A Review of Material Development and Applications. Journal of Biomimetics Biomaterials and Tissue Engineering 12 (2012) 25-39. https://doi.org/10.4028/www.scientific.net/JBBTE.12.25.

[4] Z.G. Huan , M.A. Leeflang, J. Zhou, L.E. Fratila-Apachitei, J. Duszczyk. In vitro degradation behavior and cytocompatibility of Mg–Zn–Zr alloys. Journal of Materials Science: Materials in Medicine 21 (2010) 2623–2635. https://doi.org/10.1007/s10856-010-4111-8.

[5] Y. L. Cheng, T. W. QIN, H. M. WANG, Z. ZHANG, Comparison of corrosion behaviors of AZ31, AZ91, AM60 and ZK60 magnesium alloys, Transactions of Nonferrous Metals Society of China 19 (2009) 517-524. https://doi.org/10.1016/S1003-6326(08)60305-2.

[6] C. Wang, M. Sun,F. Zheng, L. Peng, W. Ding, Improvement in grain refinement efficiency of Mg–Zr master alloy for magnesium alloy by friction stir processing. Journal of Magnesium and Alloys 2 (2014) 239-244. https://doi.org/10.1016/j.jma.2014.09.001.

[7] M. Erinc, W. H. Sillekens, R. Mannens, R. J. Werkhoven, Applicability of existing magnesium alloys as biomedical implant materials, Magnesium Technology (2009) 209–214. http://resolver.tudelft.nl/uuid:4872dafb-0680-47c0-8751-bdce953b4cfe.

[8] S. Virtanen, Biodegradable Mg and Mg alloys: Corrosion and biocompatibility, Materials Science and Engineering B 176 (2011) 1600 – 1608. https://doi.org/10.1016/j.mseb.2011.05.028.

[9] W. Li, N. Li, Y. Zheng, G. Yuan, 2016, Fretting properties of biodegradable Mg-Nd-Zn-Zr alloy in air and in Hank's solution, Scientific Reports 6, 35803. https://dx.doi.org/10.1038%2Fsrep35803.

[10] Gh. B. Darband, M. Aliofkhazraei, P. Hamghalam, N. Valizade, Plasma electrolytic oxidation of magnesium and its alloys: Mechanism, properties and applications, Journal of Magnesium and Alloys 5 (2017) 74–132. https://doi.org/10.1016/j.jma.2017.02.004.

[11] V. L. Popov , Contact mechanics and Friction: Physical Principles and Applications. Springer. Berlin, 2009.

[12] L. Pezzato, M. Rigona, A. Martuccia, K. Brunellia, M. Dabalà, Plasma Electrolytic Oxidation (PEO) as pre-treatment for sol-gel coating on aluminum and magnesium alloys, Surface and Coatings Technology 366 (2019) 114-123. https://doi.org/10.1016/j.surfcoat.2019.03.023.

[13] S.V. Lamaka, G. Knörnschild, D.V.Snihirova, M.G.S.Ferreira, Complex anticorrosion coating for ZK30 magnesium alloy. Electrochimica Acta 55 (2009) 131-141. https://doi.org/10.1016/j.electacta.2009.08.018.

[14] H. Li, S. Lu, W. Qin, L. Han, X. Wu, Improving the wear properties of AZ31 magnesium alloy under vacuum low-temperature condition by plasma electrolytic oxidation coating, Acta Astronautica 116 (2015) 126–131. https://doi.org/10.1016/j.actaastro.2015.07.005.

[15] A. Kossenko, M. Zinigrad, A universal electrolyte for the plasma electrolytic oxidation of aluminum and magnesium alloys, Materials and Design 88 (2015) 302–309. https://doi.org/10.1016/j.matdes.2015.08.071.

[16] R. B. Heimann, 2021. Magnesium Alloys for Biomedical Application: Advanced corrosion control through surface coating, Surface and Coatings Technology 405 , 126521. https://doi.org/10.1016/j.surfcoat.2020.126521.

[17] R.O. Hussein, D.O. Northwood, X. Nie, The effect of processing parameters and substrate composition on the corrosion resistance of plasma electrolytic oxidation (PEO) coated magnesium alloys, Surface and Coatings Technology 237 (2013) 357-368. http://dx.doi.org/10.1016/j.surfcoat.2013.09.021.

[18] K.O. Gunduz, Z.C. Oter, M. Tarakci, Y. Gencer, Plasma electrolytic oxidation of binary Mg-Al and Mg-Zn alloys, Surface and Coatings Technology 323 (2017) 72-81. http://dx.doi.org/10.1016/j.surfcoat.2016.08.040 .

[19] H. Duan, C. Yan, F. Wang, Effect of electrolyte additives on performance of plasma electrolytic oxidation films formed on magnesium alloy AZ91D. Electrochimica Acta 52 (2007) 3785–3793. https://doi.org/10.1016/j.electacta.2006.10.066.

[20] D. Kajáneka, B. Hadzima, J. Buhagiar , J. Wasserbauer , M. Jacková. Corrosion degradation of AZ31 magnesium alloy coated by plasma electrolytic oxidation. Transportation Research Procedia 40 (2019) 51–58. https://doi.org/10.1016/j.trpro.2019.07.010.

[21] S. Lu, Z.X. Wang, J. Chen, X.S. Zhou, Optimization of dual electrolyte and characteristic of micro-arc oxidation coating fabricated on ZK60 Mg alloy, Transactions of Nonferrous Metals Society of China 21 (2011) 929-935. https://doi.org/10.1016/S1003-6326(11)60803-0.

[22] S. Peibo, W. Xiaohong, J. Zhaohua, Plasma electrolytic oxidation of a low friction casting on ZK60 magnesium alloy, Materials Letters 62 (2008) 3124–3126. doi: https://doi.org/10.1016/j.matlet.2008.02.023.

[23] M. Mohedano, B.J.C. Luthringer, B. Mingo, R. Arrabal, P.J. Sanchez-Egido, C. Blawert, R. Willumeit-Römer, M.L.Zheludkevich, E. Matykina, Bioactive plasma electrolytic oxidation coatings on Mg-Ca alloy to control degradation behaviour, Surface and Coating Technology 315 (2017) 454-567. https://doi.org/10.1016/j.surfcoat.2017.02.050.

[24] M.J. Shen, X.J. Wang, M.F. Zhang, High-compactness coating grown by plasma electrolytic oxidation on AZ31 magnesium alloy in the solution of silicate–borax, Applied Surface Science 259 (2012) 362–366.

https://doi.org/10.1016/j.apsusc.2012.07.052.

[25] L. Yu, J. Cao, Y. Cheng, An improvement of the wear and corrosion resistances of AZ31 magnesium alloy by plasma electrolytic oxidation in a silicate–hexametaphosphate electrolyte with the suspension of SiC nanoparticles, Surface and Coatings Technology 276 (2015) 266–278. https://doi.org/10.1016/j.surfcoat.2015.07.014.

[26] ASTM-G31-72. Standard practice for laboratory immersion corrosion testing of metals, Annual Book of ASTM Standards. American Society for Testing and Materials, Philadephia, Pennsylvania, U S A (2004).

[27] X. Wei, L. Zhicheng, L. Pinduo, L. Shijian, X. Peng, R. Deng, Q. Zhao, 2020. Improvement in corrosion resistance and biocompatibility of AZ31 magnesium alloy by $NH^{2+}$ ions, Journal of Alloys and Compounds 824, 153832. https://doi.org/10.1016/j.jallcom.2020.153832.

[28] Y. Xin, T.Hu, P.K.Chu, In vitro studies of biomedical magnesium alloys in a simulated physiological environment: A review. Acta Biomaterialia 7 (2011) 1452–1459. https://doi.org/10.1016/j.actbio.2010.12.004.

[29] L. Cui, S. Gao, P. Li, R.C. Zeng, F. Zhang, S.Q. Li, E.H. Han, Corrosion resistance of a self-healing micro-arc oxidation/polymethyltrimethoxysilane composite coating on magnesium alloy AZ31, Corrosion Science 118 (2017) 84-95. https://doi.org/10.1016/j.corsci.2017.01.025.

[30] Z. Zhang, R. Zeng, W. Yan, C. Lin, L. Wang, Z. Wang, D. Chen, 2020. Corrosion resistance of one-step superhydrophobic polypropylene coating on magnesium hydroxide-pretreated magnesium alloy AZ31, Journal of Alloys and Compounds 821, 153515. https://doi.org/10.1016/j.jallcom.2019.153515.

[31] Z. G. Huan, M.A. Leeflang, J. Zhou, L.E. Fratila-Apachitei, J. Duszczyk, In vitro degradation behavior and cytocompatibility of Mg–Zn–Zr alloys. Journal Material Science: Material Medical 21 (2010) 2623–2635. https://doi.org/10.1007/s10856-010-4111-8 .

[32] Z. Li, S. Sun, M. Chen, B. D. Fahlman, D. Liu, H. Bi, In vitro and in vivo corrosion, mechanical properties and biocompatibility evaluation of $MgF_2$-coated Mg-Zn-Zr alloy as cancellous screws, Materials Science and Engineering C 75 (2017) 1268–1280. https://doi.org/10.1016/j.msec.2017.02.168.

[33] P. Samanta, R. Srivastava, B. Nandan, Block copolymer compatibilization driven frustrated crystallization in electrospun nanofibers of polystyrene/poly(ethylene oxide) blends, RSC Advances 8 (2018) 17989-18007. https://doi.org/10.1039/C8RA02391C.

[34] L. Zhu, X. Ke, B. Zhang, Y. Zhang, M. Sui, Self-repairing capability of magnesium alloy during the plasma electrolytic oxidation process, Journal of Alloys and Compounds 766 (2018) 88-94. https://doi.org/10.1016/j.jallcom.2018.06.315.

[35] G. Rapheal, S. Kumar, C. Blawert, Narendra B. Dahotre, Wear behavior of plasma electrolytic oxidation (PEO) and hybrid coatings of PEO and laser on MRI 230D magnesium alloy. Wear 271 (2011) 1987–1997. https://doi.org/10.1016/j.wear.2010.12.013.

[36] T.S.N.S. Narayanan, I.S. Park, H.L. Min, Strategies to improve the corrosion resistance of microarc oxidation (MAO) coated magnesium alloys for degradable implants: prospects and challenges, Progress in Materials Science 60 (2014) 1–71. https://doi.org/10.1016/j.pmatsci.2013.08.002.

[37] V. Dehnavi, W.J. Binns, J.J. Noël, D.W. Shoesmith, B.L. Luan, Growth behaviour of low-energy plasma electrolytic oxidation coatings on a magnesium alloy, Journal of Magnesium and Alloys 6 (2018) 229–237. https://doi.org/10.1016/j.jma.2018.05.008.

[38] M. Dabala, K. Brunelli, E. Napolitani, M. Magrini, Cerium-based chemical conversion coating on AZ63 magnesium alloy. Surface and Coatings Technology 172 (2003) 227–232. https://doi.org/10.1016/S0257-8972(03)00336-0.

[39] P. Zhang, X. Nie, D.O. Northwood, Influence of coating thickness on the galvanic corrosion properties of Mg oxide in an engine coolant, Surface and Coatings Technology 203 (2009) 3271–3277. https://doi.org/10.1016/j.surfcoat.2009.04.012.

[40] W Hai-lan, C. Ying-liang, L. Ling-ling, C. Zhen-hua, W. Hui-min, Z. Zhao. The anodization of ZK60 magnesium alloy in alkaline solution containing silicate and the corrosion properties of the anodized films, Applied Surface Science 253 (2007) 9387–9394. https://doi.org/10.1016/j.apsusc.2007.05.085.

[41] S. Durdu, A. Aytaç, M. Usta, Characterization and corrosion behavior of ceramic coating on magnesium by micro-arc oxidation, Journal of Alloys and Compounds 509 (2011) 8601–8606. https://doi.org/10.1016/j.jallcom.2011.06.059.

[42] Y. Savguira, T. H. North, S. J. Thorpe, Plasma electrolytic oxidation coating of dissimilar AZ31/AZ80 friction stir welds, Journal of the Electrochemical Society 165 (2018) C11–C18. https://doi.org/10.1149/2.0691802jes.

[43] R. O. Hussein, X. Nie, D.O. Northwood, An investigation of ceramic coating growth mechanisms in plasma electrolytic oxidation (PEO) processing, Electrochimica Acta 112 (2013) 111-119. https://doi.org/10.1016/j.electacta.2013.08.137.

[44] M. Liu, S. Zanna, A. Seyeux, H. Ardelean, G. Song, A. Atrens, P. Marcus, Electrochemical reactivity, surface composition and corrosion mechanisms of the complex metallic alloy Al3Mg2, Corrosion Science 52 (2010) 562-578. https://doi.org/10.1016/j.corsci.2009.10.015.

[45] G. Song, A. Atrens, Corrosion mechanisms of magnesium alloys, Advanced Engineering Materials 1 (1999) 11 - 33. https://doi.org/10.1002/(SICI)1527-2648(199909)1:1%3C11::AID-ADEM11%3E3.0.CO;2-N.

[46] G. Song, A. Atrens, D.S. John, X. Wu, J. Nairn, The anodic dissolution of magnesium in chloride and sulphate solutions, Corrosion Science 39 (1997) 1981-2004. https://doi.org/10.1016/S0010-938X(97)00090-5.

[47] Y. Xin, K. Huo, H. Tao, Guoyi Tang, Paul K.Chu, Influence of aggressive ions on the degradation behavior of biomedical magnesium alloy in physiological environment, Acta Biomaterials 4 (2008) 2008–2015. https://doi.org/10.1016/j.actbio.2008.05.014.

[48] E. Zhang, L. Xu, G. Yu, Feng Pan, Ke Yang, In vivo, evaluation of biodegradable magnesium alloy bone implant in the first 6 months implantation, Journal of Biomedical Materials Research A 90 (2009) 882–893. https://doi.org/10.1002/jbm.a.32132.

[49] S. Wang, Investigating local corrosion behavior and mechanism of MAO coated 7075 aluminum alloy, Journal of Alloys and Compounds 826 (2020) 153976. https://doi.org/10.1016/j.jallcom.2020.153976.

[50] Z. Li, Q. Kuang, X. Dong, T. Yuan, Q. Ren, X. Wang, X. Jing, Characteristics of high-performance anti-corrosion/anti-wear ceramic coatings on magnesium-lithium alloy by plasma electrolytic oxidation surface engineering, Surface and Coatings Technology 375 (2019) 600-607. https://doi.org/10.1016/j.surfcoat.2019.07.066.

[51] A. Buling, J. Zerrer, Increasing the application fields of magnesium by ultraceramic®: Corrosion and wear protection by plasma electrolytical oxidation (PEO) of Mg alloys, Surface and Coatings Technology 369 (2019) 142-155. https://doi.org/10.1016/j.surfcoat.2019.04.025.

[52] W. Xue, Z. Deng, R. Chen, T. Zhang, Growth regularity of ceramic coatings formed by microarc oxidation on Al–Cu–Mg alloy, Thin Solid Films 372 (2000) 114–117. https://doi.org/10.1016/S0040-6090(00)01026-9.

[53] A.L. Yerokhin, X. Nie, A. Leyland, A. Matthews, S.J. Dowey, Plasma electrolysis for surface engineering, Surface and Coating Technology 122 (1999) 73–93. https://doi.org/10.1016/S0257-8972(99)00441-7.

[54] H. Chen, A. T. Alpas, Sliding wear map for the magnesium alloy Mg-9Al-0.9 Zn (AZ91), Wear 246 (2000) 106 – 116. https://doi.org/10.1016/S0043-1648(00)00495-6.

[55] X. Li, X. Liu, B.L. Luan, Corrosion and wear properties of PEO coatings formed on AM60B alloy in $NaAlO_2$ electrolytes, Applied Surface Science 257 (2011) 9135–9141. https://doi.org/10.1016/j.apsusc.2011.05.115.

**Tables**

**Table I**: Chemical compositions of the magnesium alloys used in this study.

| Sample | at.% Mg | at.% Zr | at.% Zn | at.% V |
|---|---|---|---|---|
| ZK30 | 95.97 ± 0.20 | 0.36 ± 0.01 | 3.59 ± 0.08 | 0.04 ± 0.004 |
| ZK60 | 93.17 ± 0.22 | 0.41 ± 0.01 | 6.28 ± 0.13 | 0.05 ± 0.004 |

**Table II.** Micrometric roughness values measured by contact profilometry.

| Sample | *Ra* (µm) | *Rz* (µm) |
|---|---|---|
| ZK30 | 0.04 ± 0.01 | 0.30 ± 0.05 |
| ZK60 | 0.04 ± 0.01 | 0.24 ± 0.05 |
| ZK30PEO | 1.1 ± 0.2 | 7.9 ± 0.6 |

**List of figures captions**

**Figure 1.** SEM micrographs and EDS mapping of Mg and Zn in the uncoated ZK30 and ZK60 alloys (after polishing).

**Figure 2**. Corrosion rates determined from mass loss and $H_2$ evolution for the uncoated ZK30 and ZK60 alloys in Hank's solution for 96 h.

**Figure 3.** Morphological and structural characteristics of the PEO coating on the ZK30 alloy: optical interferometry image of the surface with 0.95 x 1.26mm analysis area (a), X-ray diffraction pattern (b), SEM image of the surface (c), and cross-sectional EDS mapping (d).

**Figure 4.** Comparison between ZK30PEO and ZK30 in hydrogen evolution volume as a function of immersion time in Hank's solution.

**Figure 5.** SVET current maps (a and c) and optical micrographs with delimitation of the mapped area (b and d) of ZK30 and ZK30PEO samples after immersion in Hank's solution for 20 min, 4 h and 24 h.

**Figure 6.** (a) Evolution of coefficient of friction (COF) with time and optical micrographs showing wear tracks (b1, b2, b3) and the spheres – counter specimens (c1, c2 and c3).

**Figure 7**. SEM images of the wear tracks (a1, a2) of ZK30 and ZK60 samples and spheres (b1, b2), with respective EDS spectra, after the tribological tests at a load of 2 N, frequency of 1 Hz, track length of 2 mm, and duration of 10 min.

**Figure 8**. SEM images of the wear track of ZK30PEO and sphere after 120 min of the tribological test and EDS spectra.

**Figure 9.** Topographic image of the wear tracks of samples ZK30 (a1), ZK60 (a2) and ZK30PEO (a3) and (b) volume of material removed, based on the calculation of the internal area of the wear tracks.

**Figure 10.** Evolution of COF till 120 min of the tribological test time (a) and SEM images of the wear tracks on ZK30PEO specimens at different test times: 10 min (b), 30 min (c), 60 min (d), and 120 min (e), showing the presence of a third body from wear (e2).

**Figures**

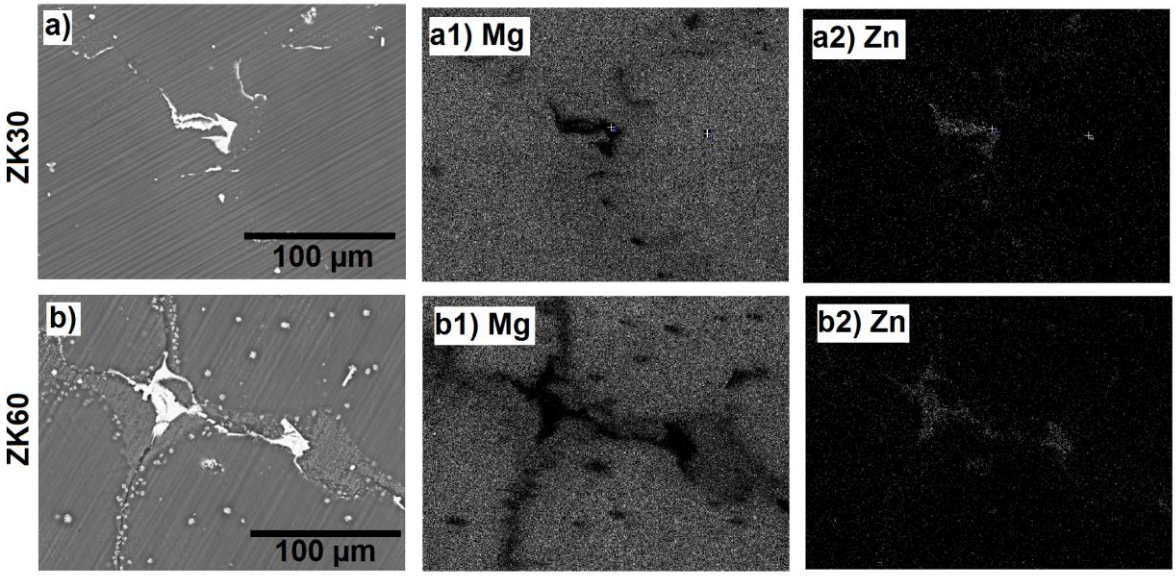


**Figure 1**

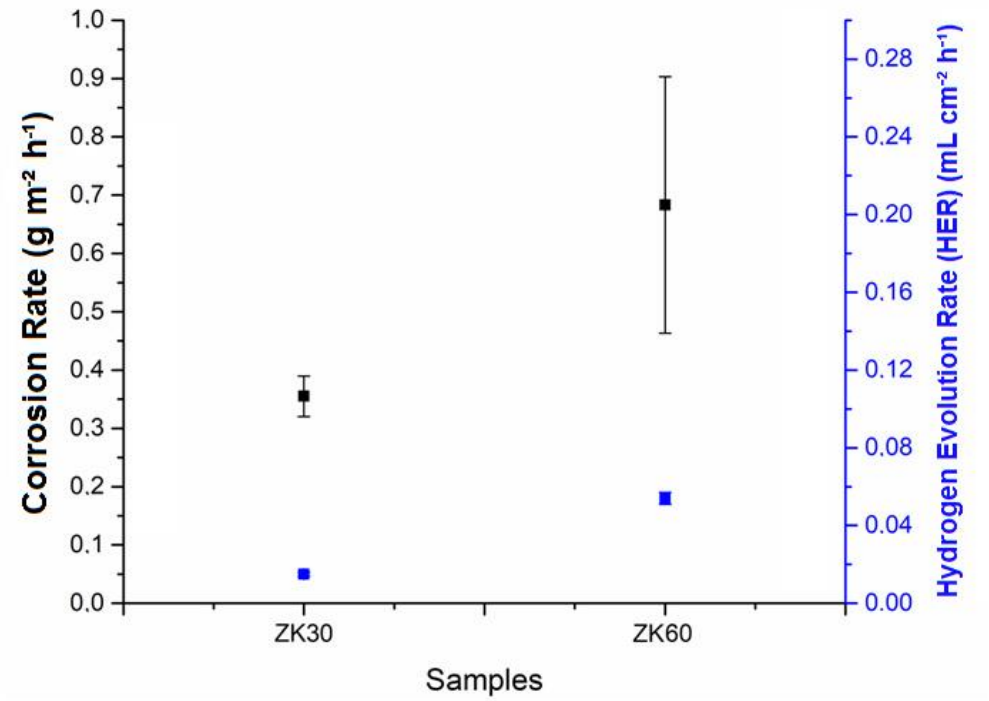


**Figure 2**

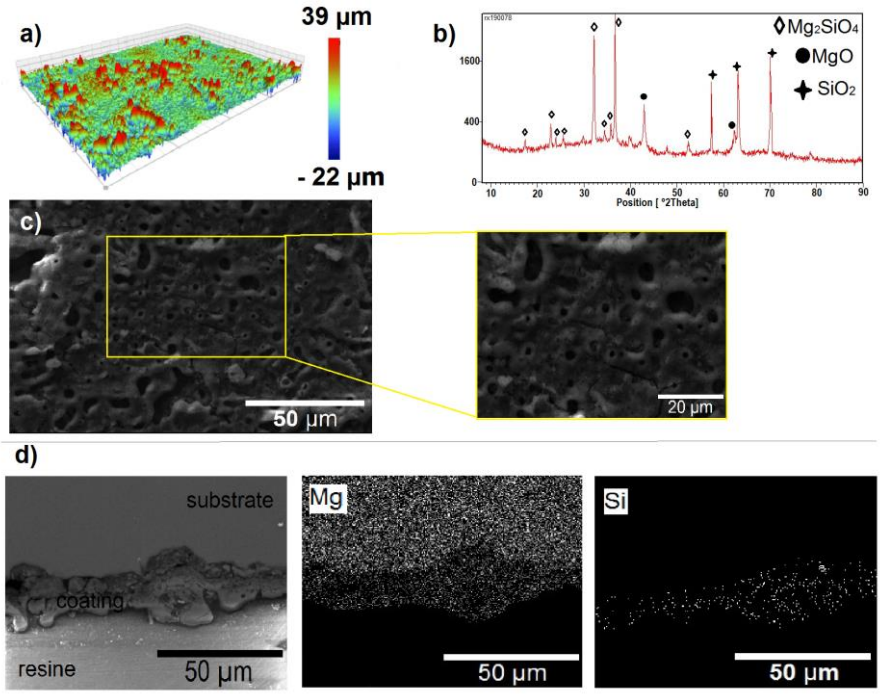


**Figure 3**

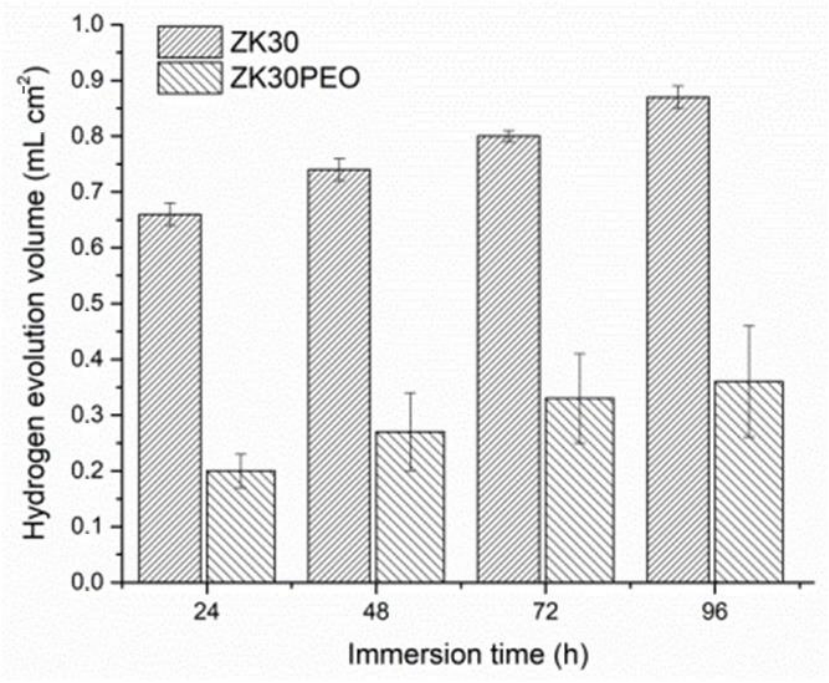


**Figure 4**

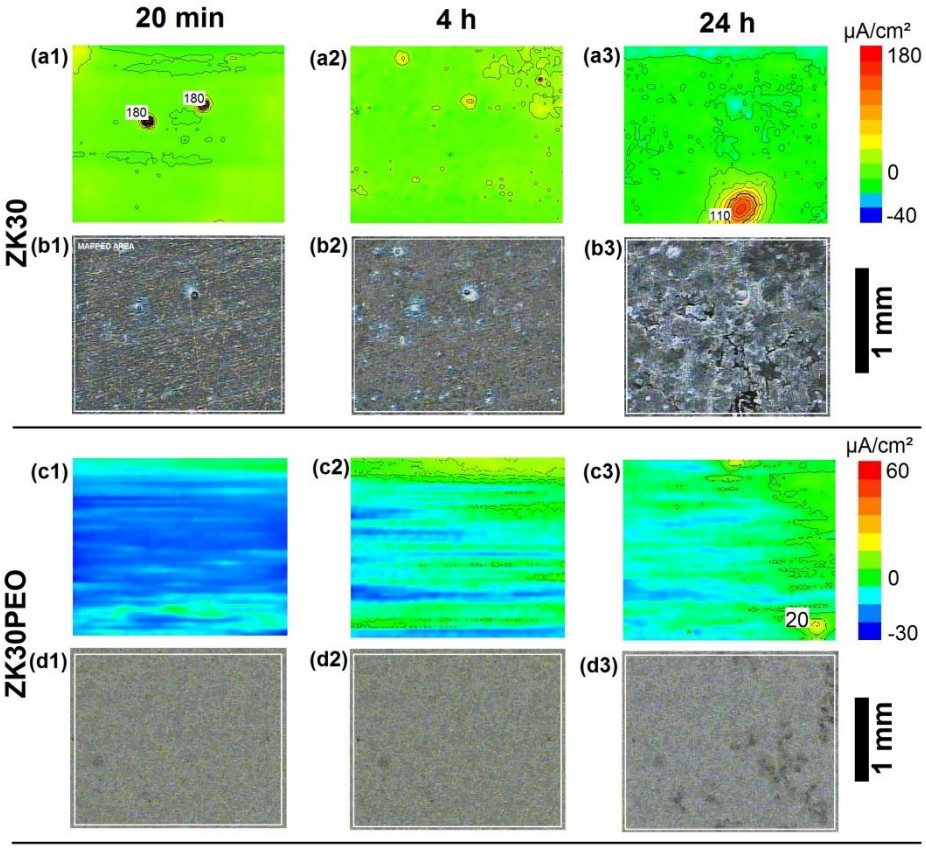
20 min
4 h
24 h
μA/cm²
180
0
-40
(a1)
(a2)
(a3)
180
180
110
ZK30
(b1)
(b2)
(b3)
MAPPED AREA
1 mm
μA/cm²
60
0
-30
(c1)
(c2)
(c3)
20
ZK30PEO
(d1)
(d2)
(d3)
1 mm

**Figure 5**

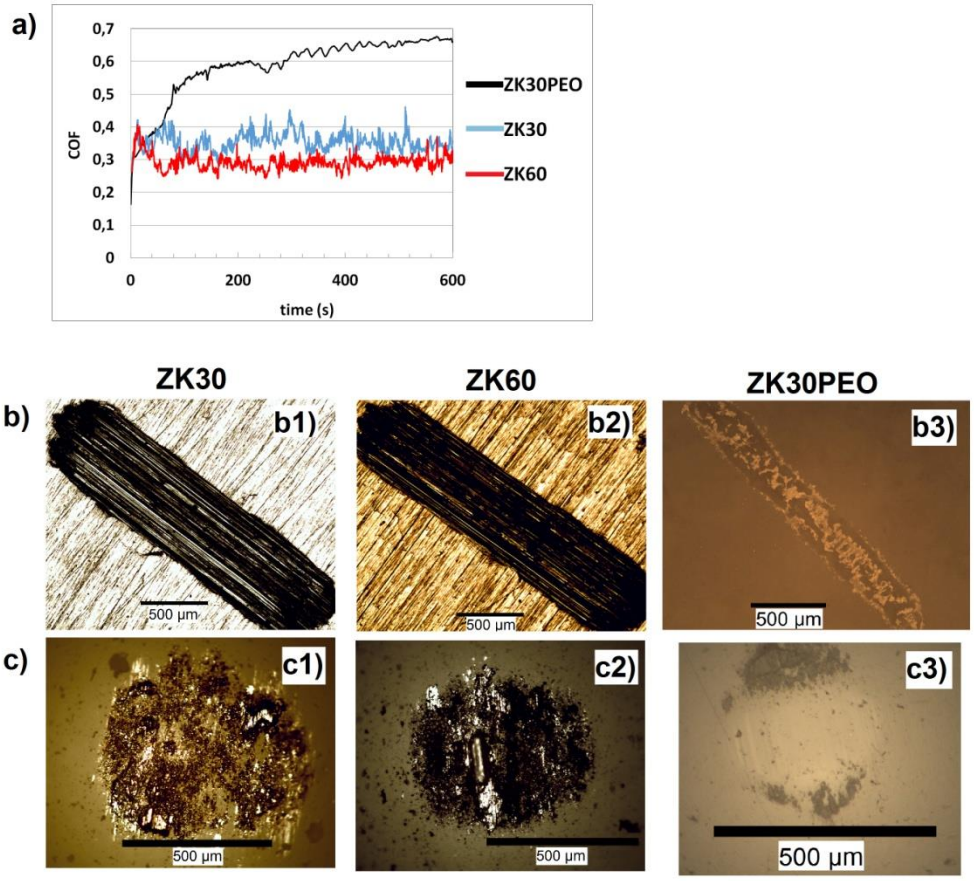
a)
0,7
0,6
0,5
0,4
0,3
0,2
0,1
0
COF
0
200
400
600
time (s)
ZK30PEO
ZK30
ZK60
ZK30
ZK60
ZK30PEO
b)
b1)
b2)
b3)
500 µm
500 µm
500 µm
c)
c1)
c2)
c3)
500 µm
500 µm
500 µm

**Figure 6**

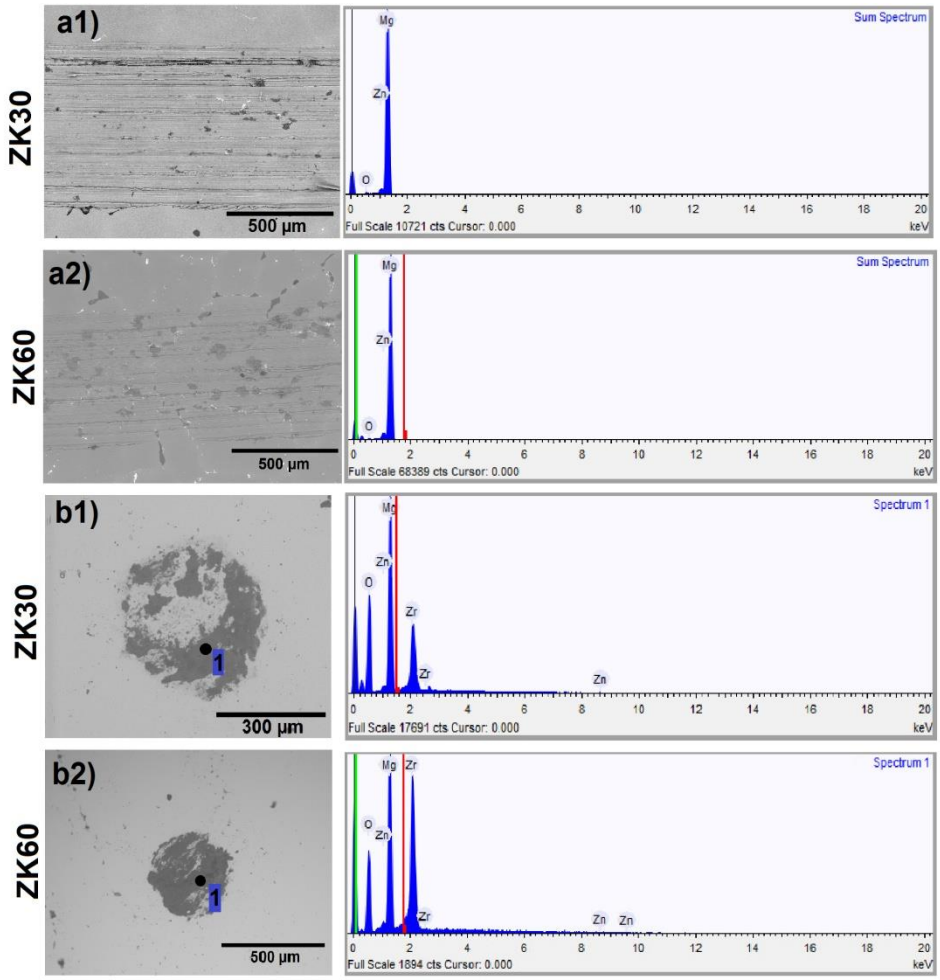
a1)
ZK30
500 µm
Mg
Zn
O
Sum Spectrum
Full Scale 10721 cts Cursor: 0.000
keV
a2)
ZK60
500 µm
Mg
Zn
O
Sum Spectrum
Full Scale 68389 cts Cursor: 0.000
keV
b1)
ZK30
1
300 µm
Mg
Zn
O
Zr
Zr
Zn
Spectrum 1
Full Scale 17691 cts Cursor: 0.000
keV
b2)
ZK60
1
500 µm
Mg
Zr
O
Zn
Zr
Zn
Zn
Spectrum 1
Full Scale 1894 cts Cursor: 0.000
keV

**Figure 7**

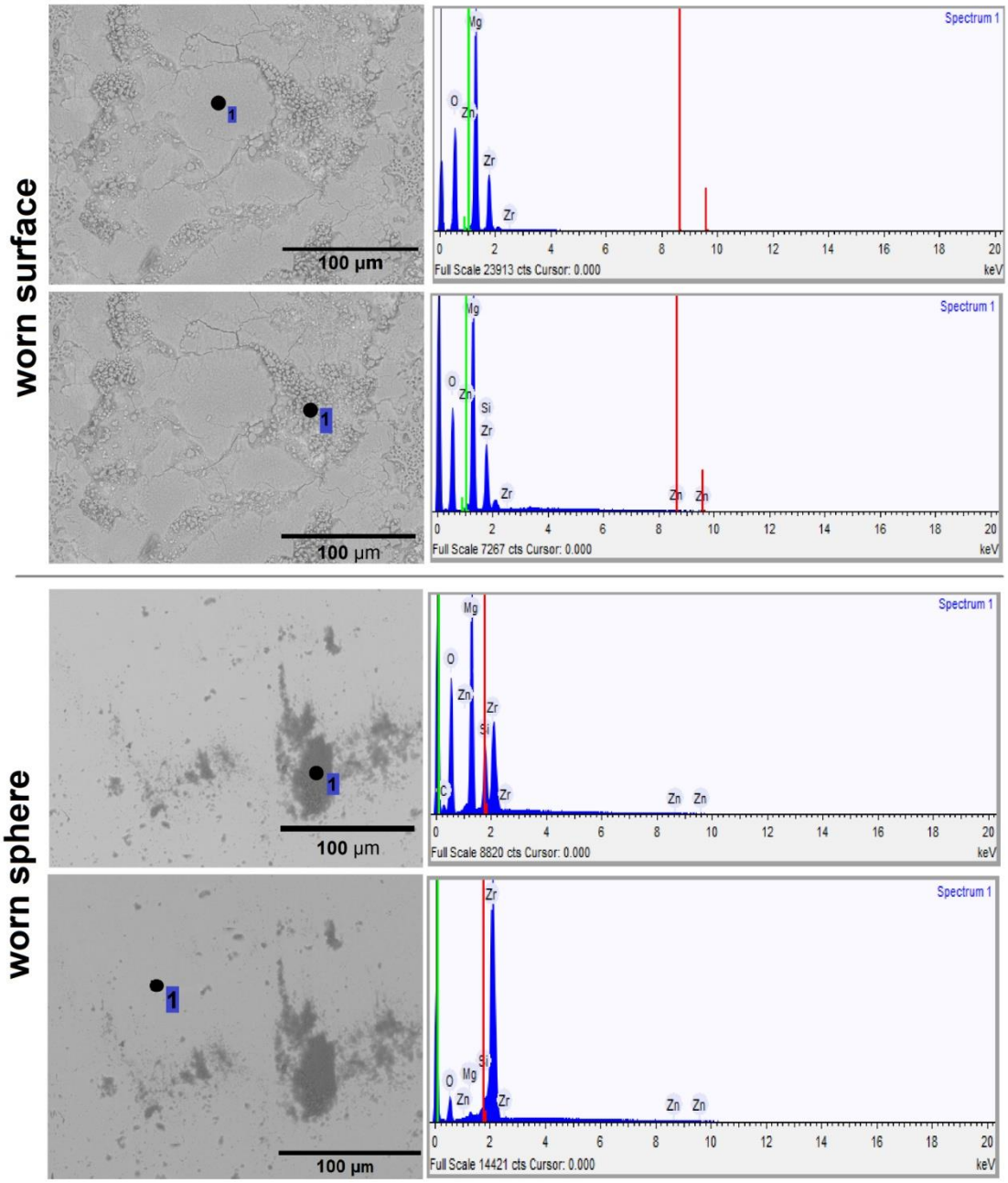
worn surface
worn sphere
100 µm
Spectrum 1
Mg
O
Zn
Zr
Si
C
Full Scale 23913 cts Cursor: 0.000
Full Scale 7267 cts Cursor: 0.000
Full Scale 8820 cts Cursor: 0.000
Full Scale 14421 cts Cursor: 0.000
keV

**Figure 8**

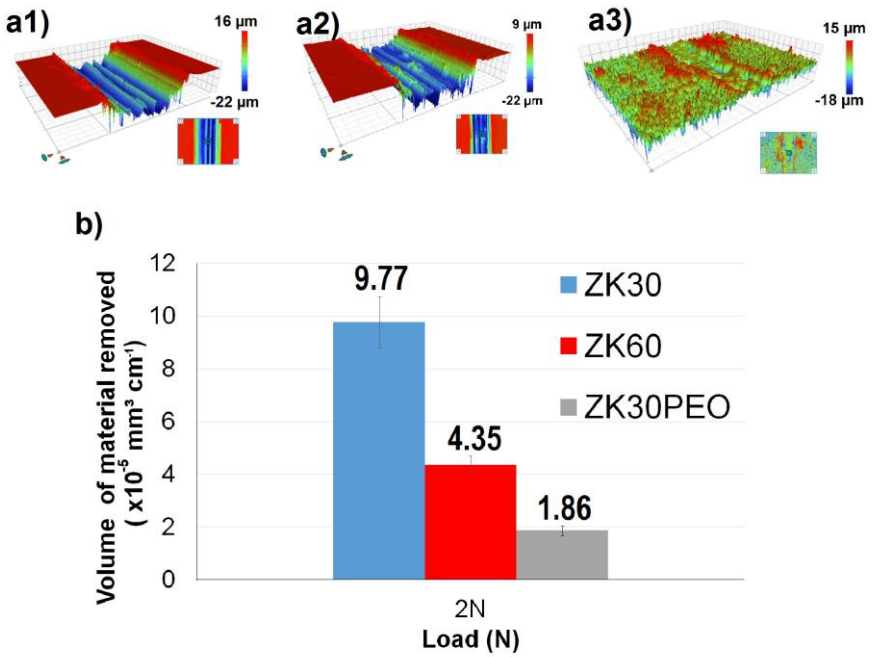
a1)
16 µm
-22 µm
a2)
9 µm
-22 µm
a3)
15 µm
-18 µm
b)
Volume of material removed
( x10-5 mm3 cm-1)
12
10
8
6
4
2
0
9.77
4.35
1.86
ZK30
ZK60
ZK30PEO
2N
Load (N)

**Figure 9**

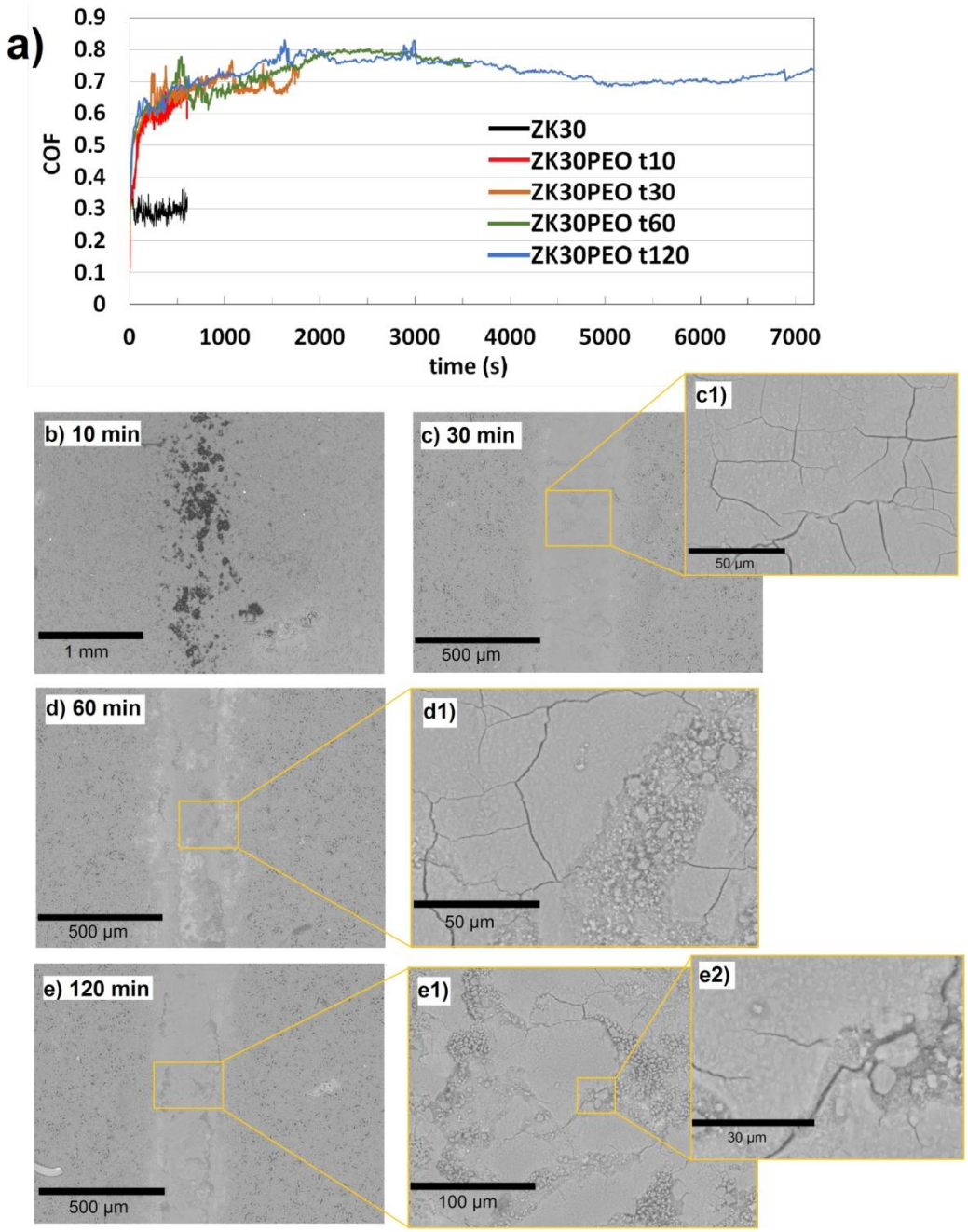
a)
COF
time (s)
ZK30
ZK30PEO t10
ZK30PEO t30
ZK30PEO t60
ZK30PEO t120
b) 10 min
1 mm
c) 30 min
500 µm
c1)
50 µm
d) 60 min
500 µm
d1)
50 µm
e) 120 min
500 µm
e1)
100 µm
e2)
30 µm

**Figure 10**